Degraded sulfated galactan derived from *Gracilaria fisheri* induces immunogenic cell death in MDA-MB-231 cells

TAWUT RUDTANATIP[1], YADA POLSAN[1], WARAPORN SAKAEW[1], SOMSUDA SOMINTARA[1], JENJIRALAI PHANPHAK[2], JAMAL EL-ABID[3], KANOKPAN WONGPRASERT[4] and CHOOWADEE PARIWATTHANAKUN[2]

[1]Electron Microscopy Unit, Department of Anatomy, Faculty of Medicine, Khon Kaen University, Khon Kaen 40002, Thailand; [2]Division of Anatomy, Faculty of Medicine, Mahasarakham University, Maha Sarakham 44000, Thailand; [3]Arrhenius Laboratory, Department of Organic Chemistry, Stockholm University, 10691 Stockholm, Sweden; [4]Department of Anatomy, Faculty of Science, Mahidol University, Bangkok 10400, Thailand

Received February 10, 2026; Accepted May 27, 2026

DOI: 10.3892/mmr.2026.13941

Abstract. Sulfated galactan (SG) isolated from *Gracilaria fisheri* has demonstrated promise for cancer therapy and prevention through inhibition of cancer cell proliferation and migration. However, its structure-activity relationship remains to be elucidated. The present study evaluated the microstructural characteristics and anticancer activity, particularly immunogenic cell death (ICD)-inducing potential, of SG and its degraded derivative (DSG) in triple-negative breast cancer cells. SG and DSG were prepared and structurally characterized using gel permeation chromatography, nuclear magnetic resonance, Fourier-transform infrared and scanning electron microscopy coupled with energy-dispersive X-ray spectroscopy. ICD induction was assessed in human MDA-MB-231 breast cancer cells using an MTT assay, phase-contrast microscopy, Hoechst/propidium iodide dual staining, intracellular reactive oxygen species (ROS) generation assay, and transmission electron microscopy (TEM). In addition, western blot analysis, immunofluorescence staining, and reverse transcription-quantitative PCR were performed. Structural analyses revealed that SG and DSG share similar backbone structures but differ markedly in sulfate content and molecular weight. Both compounds were non-toxic to normal breast epithelial MCF-10A cells and exhibited mild cytotoxicity toward MDA-MB-231 cells. DSG treatment induced notable morphological changes in cancer cells, with reduced cell numbers, increased membrane permeability and elevated intracellular ROS levels. TEM revealed DSG-induced ultrastructural changes consistent with cellular stress and cytotoxicity. DSG also markedly upregulated ICD-associated proteins [calreticulin (CRT) and Fas receptor (Fas-R)] and endoplasmic reticulum stress-related genes (protein kinase RNA-like endoplasmic reticulum kinase, inositol-requiring enzyme 1, activating transcription factor (ATF)6, ATF4, eukaryotic initiation factor 2 α subunit, CRT and Fas-R), with effects similar to the positive control doxorubicin. Therefore, these findings indicated that DSG enhances ICD in triple-negative breast cancer cells and may potentially serve as a promising ICD-inducing adjuvant for cancer immunotherapy.

Correspondence to: Professor Tawut Rudtanatip, Electron Microscopy Unit, Department of Anatomy, Faculty of Medicine, Khon Kaen University, 123 Moo 16 Thanon Mittraphap, Mueang, Khon Kaen 40002, Thailand
E-mail: tawut@kku.ac.th

Dr Choowadee Pariwatthanakun, Division of Anatomy, Faculty of Medicine, Mahasarakham University, 79/85-86 Nakornsawan Road, Muang Maha Sarakham 44000, Thailand
E-mail: choowadee@msu.ac.th

Key words: Gracilaria fisheri, degraded sulfated galactan, immunogenic cell death, triple-negative breast cancer

Introduction

Breast cancer is the most commonly diagnosed malignancy worldwide, with ~2.3 million novel cases and 685,000 mortalities reported in 2020 (1). Among its subtypes, triple-negative breast cancer, defined by the absence of estrogen receptor, progesterone receptor and HER2 expression, is the most aggressive and treatment resistant, largely due to its high metastatic potential (2). Although surgery, radiotherapy, chemotherapy, targeted therapy and immunotherapy are extensively used in breast cancer management, their effectiveness is often limited by adverse effects and suboptimal outcomes, highlighting the need for safer and more effective therapeutic strategies in the future (3).

Natural bioactive compounds have gained attention as anticancer agents due to their pleiotropic effects, ability to synergize with conventional chemotherapeutics and capacity to target multiple cancer-related pathways (4,5). For instance, medicinal plant bioactive compounds exhibit anticancer potential by suppressing the G2/M and G0/G_1 phases, inducing cell cycle arrest, and promoting apoptosis (5). Among these compounds, polysaccharides are biologically key macromolecules with

well-documented antioxidant, immunomodulatory, anticancer and anti-inflammatory properties (6-8). Since their anticancer potential was first recognized, numerous polysaccharides have been developed as adjuvant cancer therapies, including those derived from *Trametes versicolor* (synonym, *Coriolus versicolor*), fucoidan and sepia ink, which are notable for their low toxicity and favorable safety profiles (7). Sulfated galactan (SG), a polysaccharide isolated from *Gracilaria fisheri*, has been reported to inhibit the proliferation and migration of human cholangiocarcinoma HuCCA-1 cells through interaction with and inactivation of EGFR signaling (8). Furthermore, SG suppresses proliferation of human breast cancer MCF-7 cells by inducing cell cycle arrest, without cytotoxic effects on normal fibroblast L292 cells (9).

Immunotherapy has transformed cancer treatment and improved outcomes across multiple malignancies such as melanoma and breast cancer (10,11); however, majority of patients fail to respond because several tumors exhibit low intrinsic immunogenicity, enabling immune evasion (12). Immunogenic cell death (ICD) is a regulated form of cell death that increases tumor immunogenicity by promoting the release of damage-associated molecular patterns (DAMPs) and activating tumor-specific immune responses within the tumor microenvironment. Beyond direct tumor cell killing, ICD inducers enhance tumor antigenicity and adjuvanticity, thereby stimulating both innate and adaptive antitumor immunity (13,14). ICD is primarily driven by endoplasmic reticulum (ER) stress and/or reactive oxygen species (ROS), leading to the exposure or release of key DAMPs, such as calreticulin (CRT) (15). Furthermore, Fas receptor (Fas-R) and major histocompatibility complex class I (MHC class I) are key mediators of immune-dependent tumor cell killing and immune surveillance, with their expression levels influencing tumor sensitivity to immunotherapy (16,17).

Sulfated polysaccharides exhibit notable anti-inflammatory and immunostimulatory properties by modulating immune responses, regulating oxidative stress and inhibiting pro-inflammatory signaling pathways (18,19). Notably, SG from *Gracilaria fisheri* has been reported to enhance immunostimulatory activity in murine J774A1 macrophages by increasing the secretion of pro-inflammatory cytokines, including TNF-α, IL-1β and IL-6 (20), suggesting its potential to induce ICD. However, despite increasing evidence that supports the antiproliferative, anticancer and immunomodulatory effects of SG (8,9,20), its ability to induce ICD has not been elucidated. Furthermore, the biological activity of SG is notably dependent on its structural characteristics, particularly molecular weight (21). To date, no studies have investigated whether SG or its degraded derivative (DSG) induce ICD in triple-negative breast cancer cells, to the best of our knowledge. Therefore, the present study aimed to investigate the microstructural features and ICD-inducing effects of SG and DSG from *Gracilaria fisheri* in triple-negative breast cancer cells (MDA-MB-231).

Materials and methods

Gracilaria fisheri SG and DSG. SG and DSG were derived from *Gracilaria fisheri*, which was collected from the Shrimp Genetic Improvement Center (Surat Thani, Thailand) between October and December 2024. The polysaccharides were prepared according to previously established methods (21,22). SG had a molecular weight of 217 kDa, whereas DSG had a molecular weight of 8 kDa, as determined by gel permeation chromatography (Fig. S1). The structures of SG and DSG were confirmed by ^{1}H- and ^{13}C-nuclear magnetic resonance (Bruker Corporation) analyses. Both compounds consist of alternating 3-linked β-D-galactopyranose and 4-linked 3,6-anhydro-α-L-galactopyranose or α-L-galactopyranose-6-sulfate residues, as presented in Fig. S2, consistent with previous studies (21,22).

Analysis of surface morphology and elemental composition of SG and DSG. The surface morphology and elemental composition of SG and DSG were examined using scanning electron microscopy coupled with energy-dispersive X-ray spectroscopy (SEM-EDX). Samples (5-10 μg) were deposited onto SEM stubs and gold-coated for 2 min at a coating current of 20 mA. Surface morphology was visualized using an SEM (JSM-IT200™; JEOL, Ltd.) and elemental composition was analyzed using an EDX detector (Ultim® Max 40; Oxford Instruments plc). For EDX measurements, the accelerating voltage was set to 10 kV, with a working distance of ~8.8 mm. Spectra were acquired from randomly selected regions of each sample to ensure representative elemental characterization. At least three independent areas were analyzed and the acquisition time for each spectrum was ~30 sec. Elemental mapping and point analyses were performed using the instrument software (AZtec® version 6.1; Oxford Instruments) to identify and quantify the elemental distribution on the sample surface. The elemental composition was reported as weight (%).

Sulfate content and Fourier-transform infrared (FTIR) spectroscopy analysis. Sulfate groups in SG and DSG were quantified using the barium chloride ($BaCl_2$)-gelatin method and confirmed by FTIR spectroscopy. Samples (20 mg) were hydrolyzed with 2 N HCl at 100˚C for 2 h, centrifuged (3,000 x g, for 10 min at room temperature), and the supernatants were diluted with Milli-Q water and 0.5 N HCl. $BaCl_2$-gelatin reagent (1 ml) was added to the diluted supernatants, and the mixtures were incubated at room temperature for 30 min. Absorbance was measured at 550 nm to determine sulfate content as described previously (22). For FTIR analysis, SG and DSG (2 mg) were mixed with dried potassium bromide to prepare pellets and spectra were recorded using a Bruker TENSOR 27 spectrometer (attenuated total reflectance mode) over the range of 400-4,000 cm^{-1} at a resolution of 1 cm^{-1} with 16 scans.

Cell culture and cytotoxicity evaluation. Mammary epithelial cells (MCF-10A; cat. no. CRL-10317™) and breast cancer cells (MDA-MB-231; cat. no. HTB-26™) were obtained from the American Type Culture Collection. Cells were cultured in Dulbecco's Modified Eagle Medium (Gibco™; Thermo Fisher Scientific, Inc.) supplemented with 10% fetal bovine serum (Invitrogen; Thermo Fisher Scientific, Inc.) and 0.5 M sodium bicarbonate in a humidified incubator at 37˚C with 5% CO_2. The cytotoxicity of SG, DSG and doxorubicin [DOXO; Fresenius Kabi (Thailand) Ltd.], used as a positive control, was evaluated using the 3-(4,5-dimethylthiazol-2-yl)-2,5-diphenyl

tetrazolium bromide (MTT) assay. Cells were seeded in 96-well plates ($3x10^4$ cells/well; 200 μl per well) and cultured overnight at 37˚C. Cells were then treated with various concentrations of SG or DSG (100-1,000 μg/ml) or DOXO (0.02-1.50 μg/ml) for 24 h at 37˚C. Cell viability was assessed using the MTT assay, in which dimethyl sulfoxide (DMSO) was used to solubilize formazan crystals, and absorbance was measured at OD 595 nm. Cytotoxicity was expressed as the 50% cytotoxic concentration.

Cell morphology and membrane permeability evaluation. Morphological changes in MCF-10A and MDA-MB-231 cells following treatment with DOXO, SG or DSG were evaluated. Cells ($3x10^6$ cells/well) were seeded in 6-well plates and cultured for 24 h at 37˚C, then assigned to four groups: i) Normal control (NC); ii) DOXO (0.5 μg/ml); iii) SG (1,000 μg/ml); and iv) DSG (1,000 μg/ml). After 24 h of treatment, cell morphology was examined using phase-contrast microscopy (Leica DFC 7000 T; Leica Microsystems GmbH). Morphological changes were quantified in three randomly selected fields at x200 magnification using ImageJ software (version 1.54g; National Institutes of Health). To further assess membrane permeability in MDA-MB-231 cells, Hoechst/propidium iodide (PI) dual staining was performed. Cells ($6x10^4$ cells/well) were seeded onto round coverslips in 24-well plates and cultured for 24 h at 37˚C, followed by an additional 24 h of treatment at 37˚C with DOXO, SG or DSG. Cells were then washed with PBS and stained with Hoechst (Merck KGaA; MilliporeSigma) and PI (BioChemica; PanReac AppliChem) at a 1:1 μg/ml ratio for 30 min at room temperature in the dark. After washing, coverslips were mounted with antifade medium (Invitrogen; Thermo Fisher Scientific, Inc.) and stained cells were visualized using a confocal microscope (ZEISS LSM 800; Carl Zeiss AG), as described previously (21). PI fluorescence intensity was quantified in three randomly selected fields at x200 magnification using ImageJ software (version 1.54g; National Institutes of Health).

Intracellular ROS generation evaluation. Based on cytotoxicity, morphological and membrane permeability results, intracellular ROS generation was further assessed in MDA-MB-231 cells using an ROS detection assay kit (BioVision, Inc.; Abcam). Following treatment with DOXO, SG or DSG, cells were washed with 100 μl of ROS assay buffer and incubated with 100 μl of 1X ROS labeling solution containing the DCFH-DA fluorophore (BioVision, Inc.; Abcam) diluted in assay buffer at 37˚C for 45 min in the dark. Cells were then washed again with ROS assay buffer and fluorescence was measured immediately at excitation/emission wavelengths of 495/529 nm. Intracellular ROS levels were expressed as fold changes compared with the control.

Cell ultrastructure evaluation by transmission electron microscopy (TEM). MDA-MB-231 cells were further examined for ultrastructural changes following compound treatment using TEM analysis. After treatment with DOXO, SG or DSG, cells were fixed in Karnovsky's fixative (2.5% glutaraldehyde+2.0% paraformaldehyde, in 0.1 M sodium cacodylate buffer, pH 7.4) for 30 min at room temperature, washed with PBS and centrifuged at 1,500 x g for 1 min at 25˚C. Cells were post-fixed with 1% O_sO_4 in 0.1 M phosphate buffer for 1 h at room temperature, washed with PBS and centrifuged at 1,500 x g, for 1 min at room temperature. Cell pellets were embedded in 2% agarose for 20 min at room temperature, cut into small pieces and dehydrated using a graded ethanol series. Samples were infiltrated with propylene oxide and propylene oxide/EPON 812 mixtures, followed by pure EPON 812 overnight, then embedded and polymerized at 60˚C for 48 h. Ultrathin sections were prepared, stained with uranyl acetate and lead citrate, and examined using JEM-1010-TEM (JEOL Ltd.).

Western blotting analysis of ICD markers. After 6, 12 and 24 h of treatment, MDA-MB-231 cells were harvested and proteins were extracted using a protein lysis buffer (20 mM Tris-HCl, 100 mM NaCl, 5 mM phenylmethylsulfonyl fluoride; PMSF) supplemented with a 100X protease inhibitor solution. Protein concentration was determined using a NanoDrop™ 2000 spectrophotometer (Thermo Fisher Scientific, Inc.) by measuring absorbance at 280 nm. Equal amounts of protein (50 μg per sample) were separated by 12.5% SDS-PAGE and transferred onto nitrocellulose membranes (MilliporeSigma; Merck KGaA). Membranes were blocked with 2% BSA (cat. no. BSA-1S; Capricorn Scientific) in PBS for 2 h at room temperature and then incubated overnight at 4˚C with primary antibodies (1:1,000 dilution) against CRT (cat. no. MA5-15382), Fas-R (cat. no. MA5-32489) and MHC class I (cat. no. MA5-35712; Invitrogen; Thermo Fisher Scientific, Inc.), followed by HRP-conjugated goat anti-rabbit secondary antibody (cat. no. 31460; 1:2,000 dilution; Invitrogen; Thermo Fisher Scientific, Inc.) for 1 h at room temperature. Immunoreactive bands were visualized using Clarity™ Western ECL substrate (Bio-Rad Laboratories, Inc.). Protein expression levels were normalized to β-actin (cat. no. AF7018; Affinity Biosciences, Inc.) and quantified by densitometric analysis using Scion Image version 4.0.2 software (Scion Corporation, Frederick, MD, USA). All experiments were performed in triplicate.

Immunofluorescent staining of ICD. Immunofluorescence staining was performed to assess the expression levels and localization of CRT, Fas-R and MHC class I in MDA-MB-231 cells. Cells grown on coated round glass coverslips were treated with DOXO (0.5 μg/ml) or DSG (1,000 μg/ml). After 12 h of treatment, cells were washed with PBS and fixed with 4% paraformaldehyde for 20 min at room temperature. After washing, cells were incubated overnight at 4˚C with primary antibodies against CRT, Fas-R and MHC class I. Cells were then incubated with a FITC-conjugated goat anti-rabbit IgG secondary antibody (1:500; cat. no. 701078; Invitrogen; Thermo Fisher Scientific, Inc.) for 1 h at room temperature. Negative controls were prepared by omitting the primary antibody. Cell membranes were counterstained with CellMask™ Deep Red Plasma Membrane (cat. no. C10046; Invitrogen; Thermo Fisher Scientific, Inc.) according to the manufacturer's instructions and nuclei were stained using ProLong™ Diamond Antifade Mountant with DAPI (Invitrogen; Thermo Fisher Scientific, Inc.) for 5 min at room temperature. Immunofluorescence images were acquired using a confocal microscope (ZEISS

Table I. Primer sequences used in the present study.

Gene	Primer sequences (5'-3')
PERK	F: ATTGCATCTGCCTGGTTAC
	R: GACTCCTTCCTTTGCCTGT
IRE1	F: GACAGGCTCAATCAAATGG
	R: CGGTCAGGAGGTCAATAACA
ATF4	F: CCAGCAAAGCACCGCAACA
	R: CCATCCACAGCCAGCCATT
ATF6	F: CAGGGAGAAGGAACTTGTGA
	R: ACTGACCGAGGAGACGAGA
elF2α	F: AAGGCGTATCCGTTCTATCA
	R: CTTCCCGTTCATCTTCATTC
CRT	F: TCAAGGAGCAGTTTCTGGACGG
	R: GCATCCTGGCTTGTCTGCAAAC
Fas-R	F: TGAAGGACATGGCTTAGAAGTG
	R: GGTGCAAGGGTCACAGTGTT
MHC class I	F: CAGTTCGTGAGGTTCGACAG
	R: CAGCCGTACATGCTCTGGA
GAPDH	F: GGTGAAGGTCGGTGTGAACG
	R: CTCGCTCCTGGAAGATGGTG

F, forward; R, reverse; MHC, major histocompatibility complex; Fas-R, Fas receptor; CRT, calreticulin; PERK, protein kinase RNA-like endoplasmic reticulum kinase; ATF, activating transcription factor; IRE1, inositol-requiring enzyme 1; eIF2α, eukaryotic initiation factor 2 α subunit.

LSM 800; Carl Zeiss AG). FITC fluorescence intensity for CRT, Fas-R and MHC class I was quantified in three randomly selected fields at x200 magnification using ImageJ software (version 1.54g; National Institutes of Health).

Determination of ICD-related genes by reverse transcription-quantitative PCR (RT-qPCR) analysis. Total RNA was extracted using TRIzol® reagent (200 µl; MilliporeSigma) and RNA purity and concentration were assessed by measuring the A260/280 ratio using a NanoDrop™ 2000 spectrophotometer (Invitrogen; Thermo Fisher Scientific, Inc.). Complementary DNA (cDNA) was synthesized from 1 µg of RNA using the RevertAid™ First Strand cDNA Synthesis Kit (Invitrogen; Thermo Fisher Scientific, Inc.) by incubation at 42˚C for 60 min, followed by 70˚C for 5 min. Gene expression was analyzed by RT-qPCR using synthesized cDNA, SYBR Green PCR Master Mix (Invitrogen; Thermo Fisher Scientific, Inc.) and gene-specific forward and reverse primers. The RT-qPCR thermocycling conditions were as follows: 50˚C for 2 min, 95˚C for 10 min and 40 cycles of 95˚C for 15 sec, 60˚C for 30 sec and 72˚C for 30 sec. Relative mRNA expression levels were calculated using the $2^{-\Delta\Delta Cq}$ method (23) and analyzed using Bio-Rad CFX Maestro software version 2.3 (Bio-Rad Laboratories, Inc.). Primers targeting protein kinase RNA-like ER kinase (PERK), inositol-requiring enzyme 1 (IRE1), activating transcription factor (ATF)6, ATF4, eukaryotic initiation factor 2 α subunit (eIF2α), CRT, Fas-R, MHC class I and GAPDH were obtained from BIONICS Co., Ltd. Primer sequences were designed using National Center for Biotechnology Information Primer-Basic Local Alignment Search Tool and are listed in Table I.

Statistical analysis. Data are presented as the mean±standard error of the mean from three or more independent experiments. Statistical significance was assessed using one-way analysis of variance followed by Tukey's multiple comparison test in GraphPad Prism software (version 10.3.1.509; Dotmatics). $P<0.05$ was considered to indicate a statistically significant difference.

Results

Surface morphology and elemental composition of Gracilaria fisheri SG and DSG. SEM-EDX was used to examine the microstructure and elemental composition of SG and DSG (24). As presented in Fig. 1A and B, SG and DSG exhibited distinct surface morphologies. SG appeared as large lamellar, bundle-like fiber structures, whereas DSG consisted of shorter, fragmented sheet-like structures with irregular shapes. EDX analysis confirmed the presence of carbon, oxygen and sulfur in both samples (Fig. 1C and D). In SG, carbon, oxygen and sulfur contents were 53.25±1.17%, 44.98±1.12% and 1.77±0.09%, respectively, whereas in DSG these values were 52.73±0.36%, 45.05±0.58% and 2.23±0.43%. The sulfate contents of SG and DSG were further quantified as 11.41±0.14% and 12.92±0.07%, respectively (Fig. S1). FTIR analysis revealed characteristic absorption bands between 400 and 4,000 cm^{-1}, consistent with polysaccharide functional groups (Fig. S2). Notably, absorbance bands at 861.60, 770.07 and 708.49 cm^{-1}, corresponding to sulfate group stretching vibrations (21), were more notable in DSG (Fig. 1E and F). These results confirmed the sulfated nature of both polysaccharides and suggested that degradation to a lower molecular weight is associated with increased sulfate content within the structure.

Effects of SG and DSG on cell viability in normal breast epithelial and human breast cancer cells. The cytotoxic effects of SG and DSG on normal breast epithelial MCF-10A cells and MDA-MB-231 breast cancer cells were evaluated after 24 h of exposure and expressed as a percentage of control at concentrations ranging from 100 to 1,000 µg/ml. SG and DSG exhibited no significant cytotoxicity toward MCF-10A cells at concentrations up to 1,000 µg/ml (Fig. 2A). By contrast, both compounds significantly reduced viability in MDA-MB-231 cells at concentrations of 400-1,000 µg/ml, with DSG exhibiting greater cytotoxic potency compared with SG (Fig. 2B). The IC_{50} values for SG and DSG in MDA-MB-231 cells were 2,736.17 and 1,927.11 µg/ml, respectively, calculated from the slope and equation obtained from Fig. 2B. DOXO, used as a positive control, significantly reduced the viability of both MCF-10A and MDA-MB-231 cells, with IC_{50} values of 0.56 and 0.52 µg/ml, respectively (Fig. 2C and D). Since SG and DSG did not achieve 50% cytotoxicity at the highest concentration tested, IC_{50} values could not be determined within the experimental range. Therefore, a concentration of 1,000 µg/ml was selected for subsequent experiments.

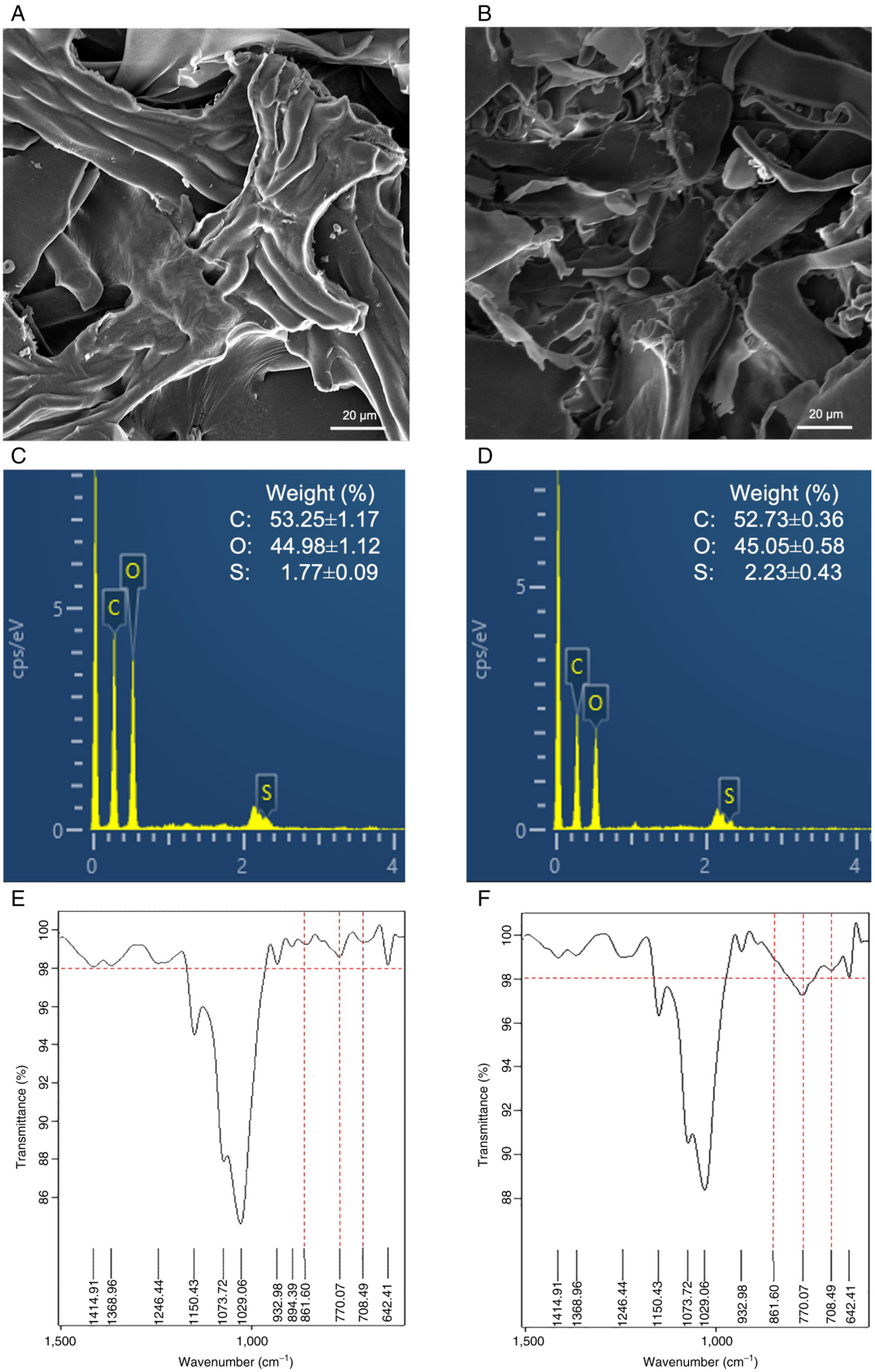

Figure 1. Surface morphology and elemental composition of SG and DSG analyzed by scanning electron microscopy coupled with energy-dispersive X-ray spectroscopy (SEM-EDX). (A) SEM micrographs indicating the microstructure of SG and (B) SEM micrographs indicating the microstructure of DSG (scale bar, 20 μm). (C) EDX spectra and corresponding elemental composition (%) of SG and (D) EDX spectra and corresponding elemental composition (%) of DSG. (E) FTIR spectra of SG and (F) FTIR spectra of DSG. The red dashed lines indicate absorbance bands corresponding to sulfate group stretching vibrations. C, carbon; O, oxygen; S, sulfur; SG, sulfated galactan; DSG, degraded sulfated galactan; SEM, scanning electron microscopy; EDX, energy-dispersive X-ray spectroscopy; FTIR, Fourier-transform infrared.

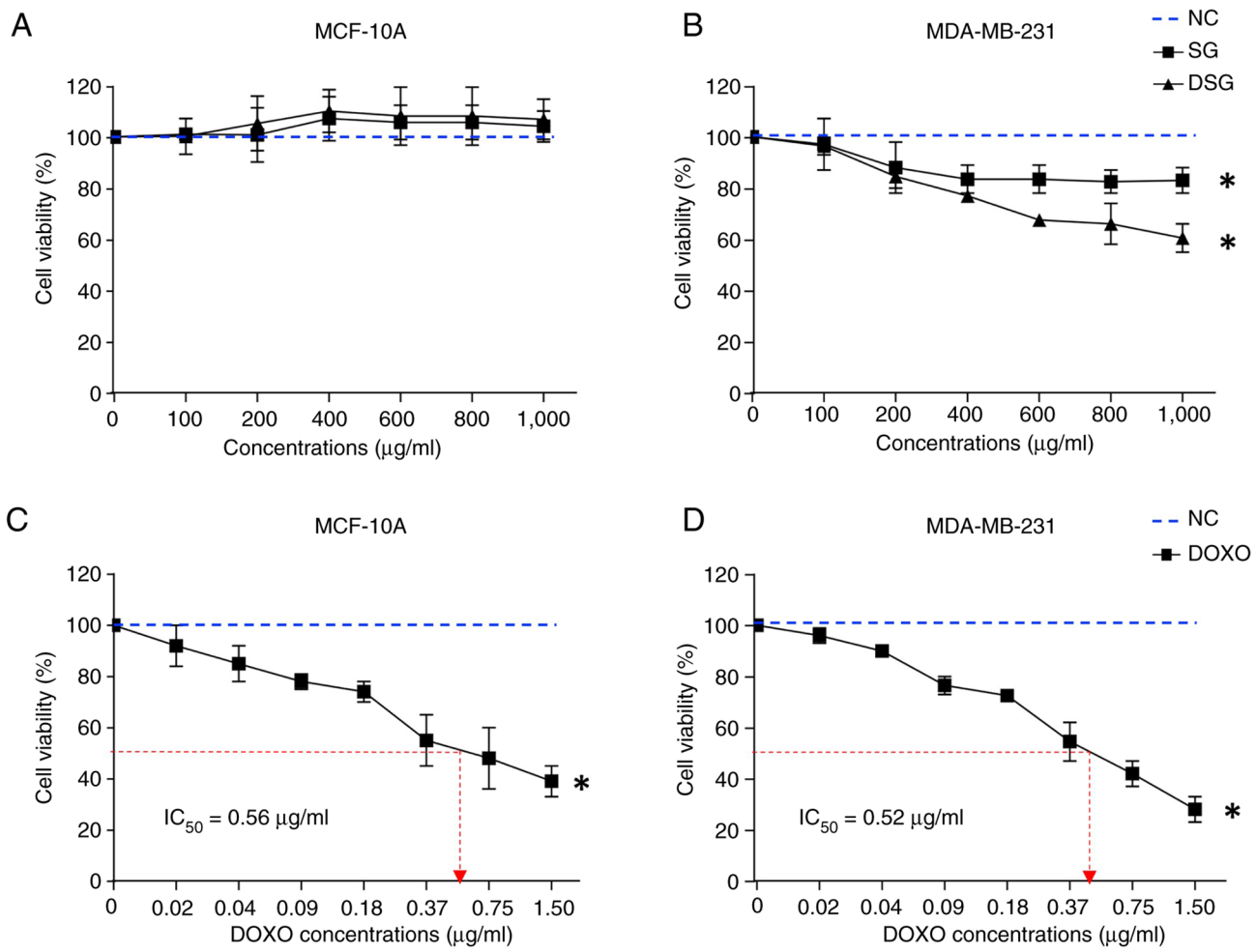

Figure 2. Effects of SG and DSG (100-1,000 μg/ml) and DOXO (0.02-1.50 μg/ml) on the viability of normal breast MCF-10A cells and breast cancer MDA-MB-231 cells, as assessed by the MTT assay. Viability of (A) MCF-10A cells treated with SG and DSG, (B) MDA-MB-231 cells treated with SG and DSG, (C) MCF-10A cells treated with DOXO and (D) MDA-MB-231 cells treated with DOXO. The red dashed lines indicate the IC50 values of DOXO in MCF-10A and MDA-MB231 cells. Results are presented as the mean±standard error of the mean (n=3) from three independent experiments. *P<0.05 indicates a statistically significant difference compared with the NC group (blue dotted lines). NC, normal control; SG, sulfated galactan; DSG, degraded sulfated galactan; DOXO, doxorubicin.

Effects of SG and DSG on morphology and intracellular ROS generation in MDA-MB-231 cells. To assess the effects of SG and DSG on cellular morphology, morphological features and membrane permeability in MDA-MB-231 cells were examined. Phase-contrast microscopy revealed that MDA-MB-231 cells treated with DOXO, SG and DSG (Fig. 3A) exhibited clear morphological changes compared with untreated controls, including cell shrinkage, rounding and detachment. By contrast, MCF-10A cells treated with SG or DSG indicated no noticeable morphological alterations compared with controls (Fig. S3). As presented in Fig. 3B, MDA-MB-231 cells treated with SG and DSG displayed prominent cytoplasmic PI fluorescence, similar to that observed in DOXO-treated cells, indicating increased membrane permeability consistent with cell death. Quantitative analysis of morphological changes and PI fluorescence intensity in MDA-MB-231 cells demonstrated a significantly higher incidence in the order of DOXO>DSG>SG (Fig. 3C and D).

Furthermore, ROS levels exceeding the antioxidant capacity of cancer cells can cause biomolecular damage and trigger cell death (25). The present study evaluated whether SG and DSG increase intracellular ROS levels. The effects of DOXO, SG and DSG on intracellular ROS generation in MDA-MB-231 cells are presented in Fig. 3E. Cells treated with DOXO and DSG exhibited significantly higher ROS levels (1.62-fold for DOXO and 1.41-fold for DSG compared with the control), whereas SG-treated cells exhibited ROS levels similar to those of the control. These findings suggested that DSG induces changes in cell morphology and membrane permeability in MDA-MB-231 cells through increased intracellular ROS generation.

Ultrastructural alterations in MDA-MB-231 cells induced by SG and DSG. To further characterize the ultrastructural effects of SG and DSG on MDA-MB-231 cells, TEM analysis was performed. As presented in Fig. 4, distinct ultrastructural differences were observed among the NC, DOXO-, SG- and DSG-treated groups. Cells in the NC group exhibited well-preserved cellular architecture, including intact nuclear membranes, prominent nucleoli, evenly distributed chromatin and a uniform, electron-lucent cytoplasm (Fig. 4A). By contrast, DOXO-treated cells

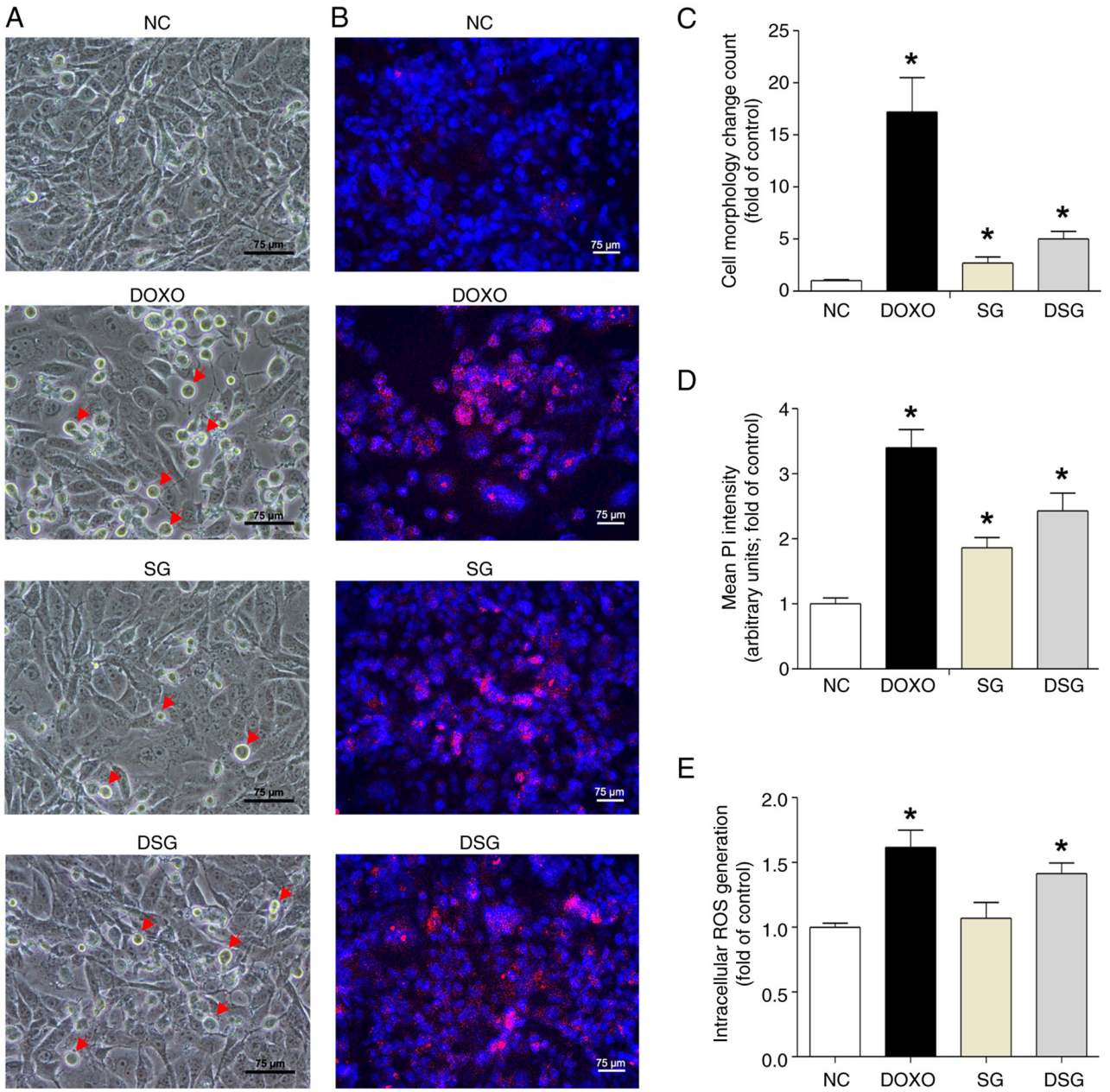

Figure 3. Cell morphology, membrane permeability alterations and intracellular ROS generation in MDA-MB-231 cells following treatment with DOXO (0.5 μg/ml), SG and DSG (both 1,000 μg/ml) for 24 h. (A) Phase-contrast micrographs exhibiting morphological features of MDA-MB-231 cells after treatment; red arrows indicate cells exhibiting morphological changes (scale bar, 75 μm). (B) Immunofluorescence micrographs indicating Hoechst and PI dual staining in MDA-MB-231 cells after treatment (scale bar, 75 μm). (C) Quantitative analysis of morphological changes in MDA-MB-231 cells treated with DOXO, SG and DSG. (D) Quantitative analysis of PI penetration intensity in MDA-MB-231 cells treated with DOXO, SG and DSG. (E) Quantitative analysis of intracellular ROS generation in MDA-MB-231 cells after treatment with DOXO, SG and DSG. Results are presented as the mean±standard error of the mean (n=3) from three independent experiments. *P<0.05 indicates a statistically significant difference compared with the NC group. SG, sulfated galactan; DSG, degraded sulfated galactan; NC, normal control; ROS, reactive oxygen species; DOXO, doxorubicin; PI, propidium iodide.

revealed marked ultrastructural damage, characterized by cytoplasmic condensation, extensive vacuolization and accumulation of electron-dense bodies, consistent with severe cellular stress and cytotoxicity (Fig. 4B). SG-treated cells largely maintained ultrastructural features similar to those of the NC group, indicating minimal cytotoxic effects (Fig. 4C). By contrast, DSG-treated cells retained nuclear integrity but exhibited notable cytoplasmic alterations, including extensive vacuolization, electron-dense inclusions and organelle disorganization (Fig. 4D). These findings indicated that DSG induces notable ultrastructural damage in MDA-MB-231 cells, with cytotoxic effects similar to those observed with DOXO.

Effects of DSG on ICD and its underlying mechanisms in MDA-MB-231 cells. ICD is a regulated form of cell death that stimulates tumor-specific immunity through the release of DAMPs from dying cancer cells, thereby activating immune responses within the tumor microenvironment. ICD can be induced by several conventional therapies, including chemotherapy, targeted therapy, radiotherapy and photodynamic therapy (15). Therefore, the present study examined the effects

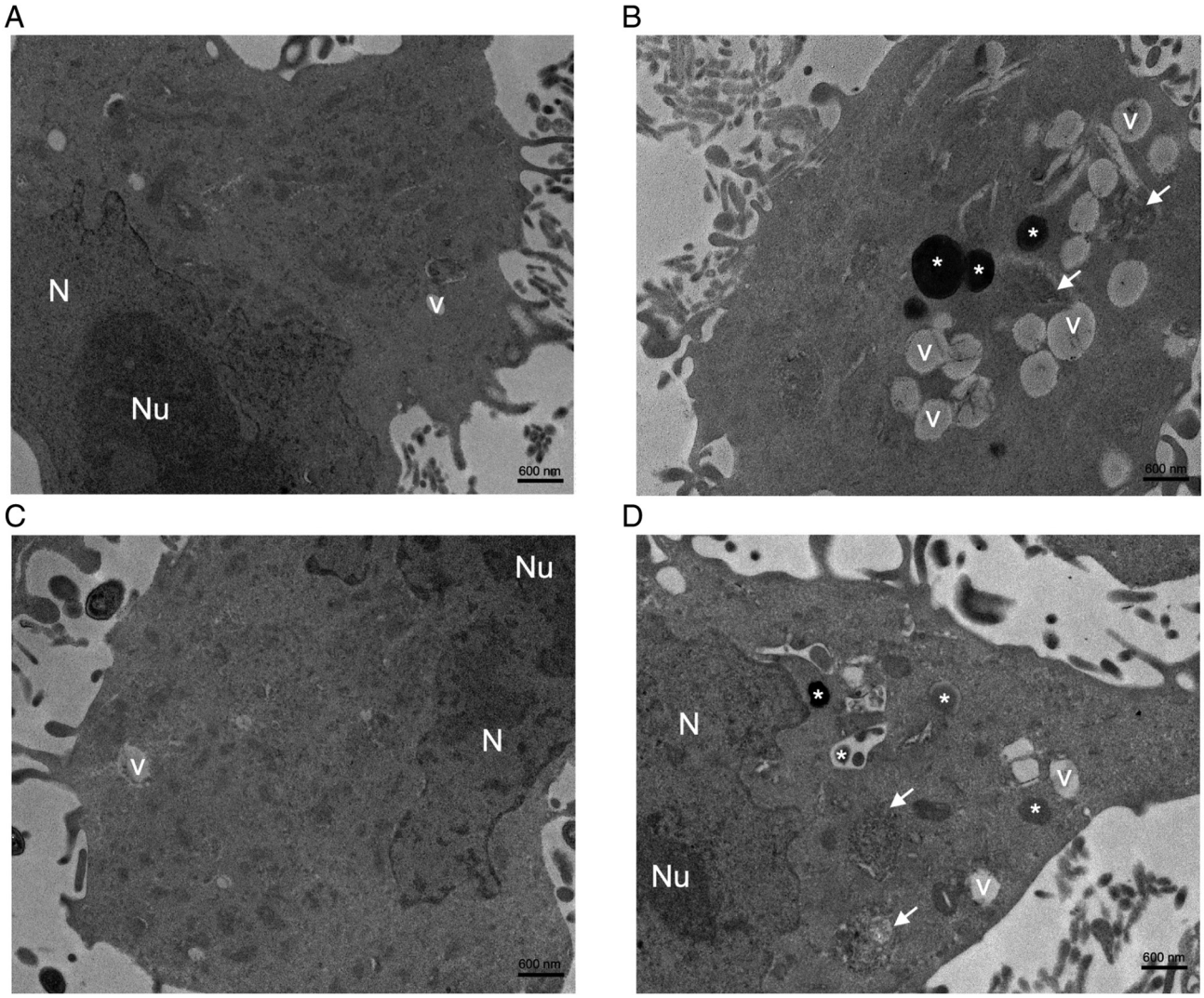

Figure 4. TEM micrographs of cultured MDA-MB-231 cells after treatment with DOXO (0.5 μg/ml), SG and DSG (both 1,000 μg/ml) for 24 h. TEM micrographs indicate (A) NC (scale bar, 600 nm), (B) DOXO-treated MDA-MB-231 cells (scale bar, 600 nm), (C) SG-treated MDA-MB-231 cells (scale bar, 600 nm) and (D) DSG-treated MDA-MB-231 cells (scale bar, 600 nm). SG, sulfated galactan; DSG, degraded sulfated galactan; N, nucleus; Nu, nucleolus; V, vacuole; *, electron-dense bodies; white arrow, organelle disorganization; TEM, transmission electron microscopy.

of DSG on ICD-related marker expression and the underlying mechanisms in MDA-MB-231 cells. DSG treatment increased the expression levels of CRT and Fas-R, as presented in Figs. 5 and 6. Western blotting analysis demonstrated that DSG significantly upregulated CRT and Fas-R expression levels at 12 and 24 h, whereas expression level of MHC class I did not differ compared with that in control cells (Fig. 5). The DSG-induced increases in CRT and Fas-R expression levels were similar to those observed in DOXO-treated cells, a known ICD inducer (26). Specifically, CRT expression increased to 1.46±0.41-fold at 6 h, 1.39±0.24-fold at 12 h and 2.09±0.26-fold at 24 h following DSG treatment compared with the control. Fas-R expression increased to 1.38±0.09-fold at 12 h and 2.14±0.74-fold at 24 h following DSG treatment.

Furthermore, confocal immunofluorescence staining was performed to confirm the expression levels and subcellular localization of CRT, Fas-R and MHC class I in MDA-MB-231 cells. Immunoreactivity of CRT and Fas-R was markedly increased in cells treated with DOXO and DSG compared with control cells, with both proteins predominantly localized at the cell surface membrane. By contrast, no significant differences in MHC class I immunoreactivity were observed among the experimental groups (Fig. 6). Quantitative analysis of FITC fluorescence intensity further revealed that DSG significantly increased CRT and Fas-R expression compared with the control (Fig. 6D), supporting the ICD-inducing activity of DSG in MDA-MB-231 cells.

Furthermore, the expression levels of key mRNAs involved in ICD-inducing mechanisms in MDA-MB-231 cells, including those associated with ER stress (15), was evaluated after DSG treatment using RT-qPCR. Compared with the control group, DSG-treated cells exhibited significant upregulation of ER stress- and ICD-related genes, including PERK, IRE1, ATF6, ATF4, eIF2α, CRT and Fas-R, consistent with the effects observed in DOXO-treated cells. By contrast, MHC class I mRNA expression remained unchanged following DSG treatment (Fig. 7). Collectively, these results indicated that DSG is associated with activation ER stress-related ICD signaling pathways at the transcriptional level, supporting its ICD-inducing potential in MDA-MB-231 breast cancer cells.

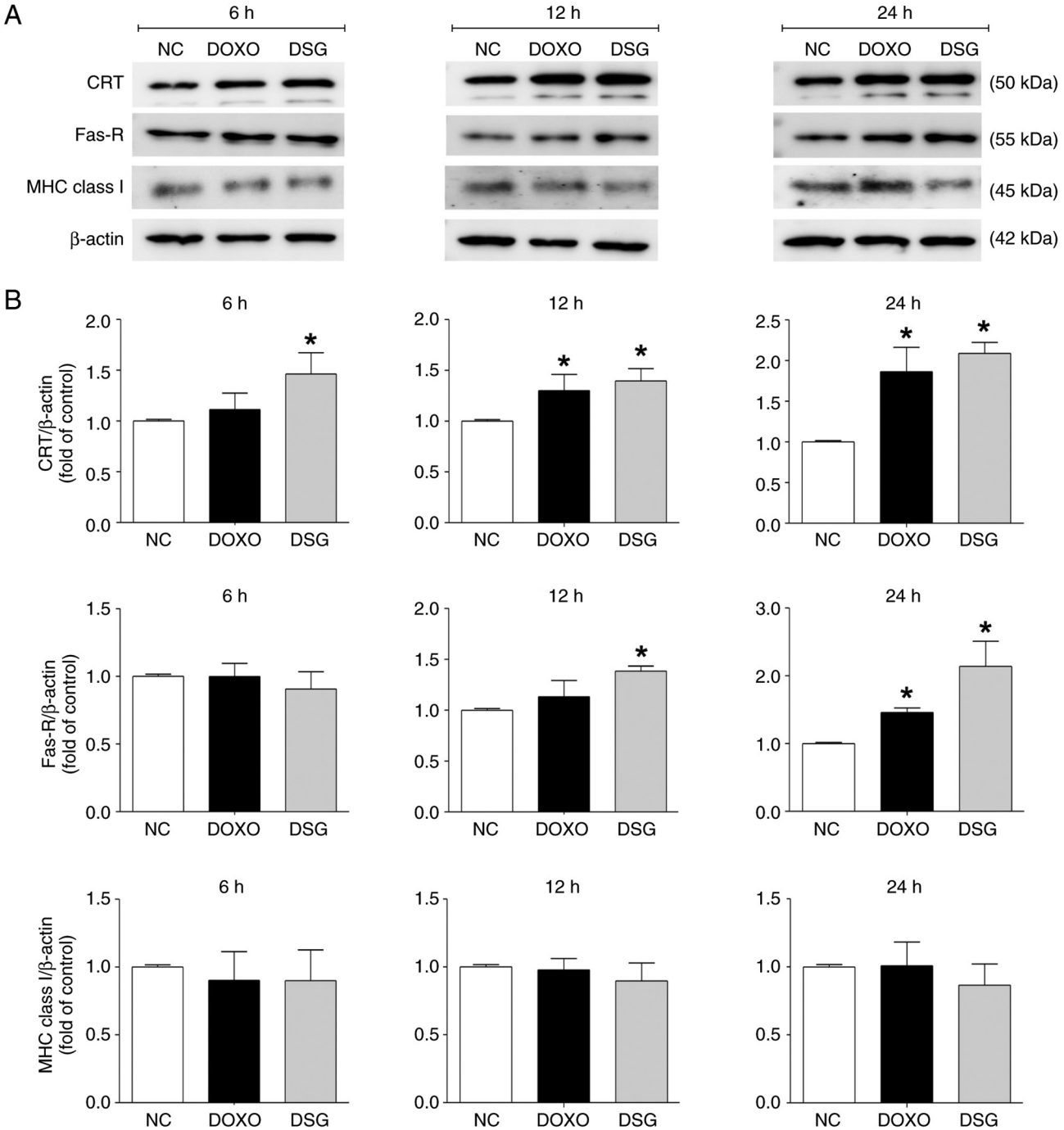

Figure 5. Expression levels of immunogenic cell death-related proteins in MDA-MB-231 cells treated with DOXO and DSG for 6, 12 and 24 h, as assessed by western blotting analysis. (A) Representative immunoblot bands of CRT, Fas-R and MHC class I in MDA-MB-231 cells from the experimental groups (NC, DOXO and DSG). (B) Quantitative analysis of CRT, Fas-R and MHC class I expression levels normalized to β-actin, with fold changes calculated relative to the NC. Results are presented as the mean±standard error of the mean (n=3) from three independent experiments. *P<0.05 indicates a statistically significant difference compared with the NC group. DSG, degraded sulfated galactan; NC, normal control; DOXO, doxorubicin; CRT, calreticulin; Fas-R, Fas receptor; MHC, major histocompatibility complex.

Discussion

There is growing interest in the anticancer potential of sulfated polysaccharides, including their application in cancer immunotherapy (18,27). Their structural diversity, extensive biological activity and notably low toxicity make sulfated polysaccharides key candidates for anticancer development. Key structural features, such as molecular weight, polysaccharide type and degree of substitution, strongly influence their biological effects (28). In particular, reduced molecular weight combined with increased sulfation has been reported to enhance polysaccharide bioactivity (29). To generate low-molecular weight SG from *Gracilaria fisheri*, acid hydrolysis has been used to produce a homogeneous DSG (21). In the present study, the surface morphology and elemental composition of SG and DSG were characterized using SEM-EDX analysis. To the best of our knowledge, the present study also provides the first evidence that DSG induces

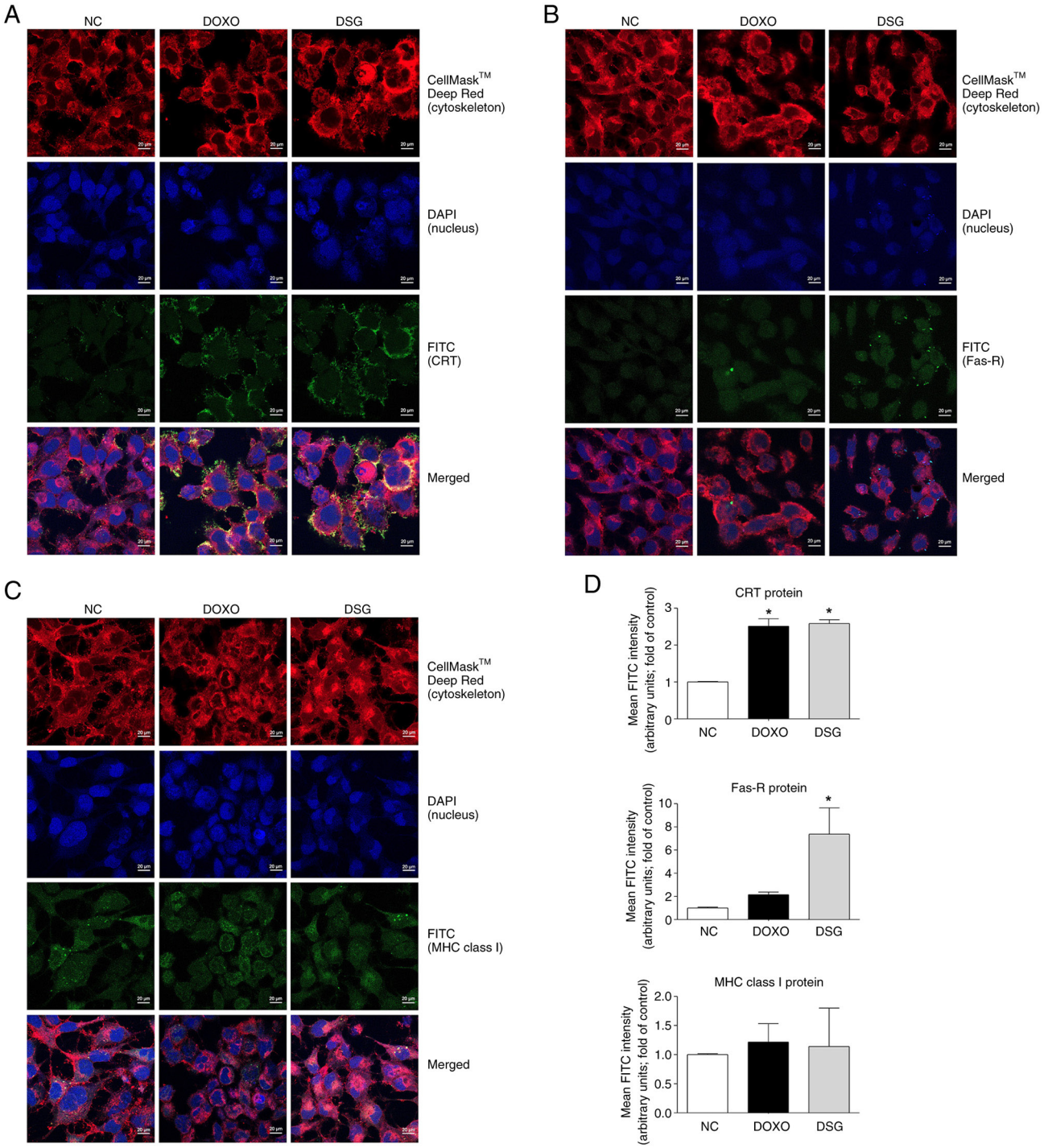

Figure 6. Expression and localization of immunogenic cell death-related proteins in MDA-MB-231 cells treated with DOXO and DSG for 12 h, as assessed by immunofluorescence staining. Confocal immunofluorescence micrographs indicate the expression and subcellular localization of CRT (A), Fas-R (B) and MHC class I (C) in MDA-MB-231 cells following treatment. Target proteins (CRT, Fas-R and MHC class I) are shown in green, nuclei are stained with DAPI (blue) and the plasma membrane is stained with CellMask™ Deep Red (red) (Scale bar, 20 μm). (D) Quantitative analysis of FITC fluorescence intensity for CRT, Fas-R and MHC class I in MDA-MB-231 cells following treatment. Data are presented as the mean±standard error of the mean (n=3) from three independent experiments. *P<0.05 indicates a statistically significant difference compared with the NC group. DSG, degraded sulfated galactan; NC, normal control; DOXO, doxorubicin; CRT, calreticulin; Fas-R, Fas receptor; MHC, major histocompatibility complex.

ICD in triple-negative breast cancer MDA-MB-231 cells. SEM is extensively used to examine the morphology and microstructural features of polysaccharides (30,31), while SEM-EDX allows simultaneous assessment of microstructure and elemental composition (24,32). The SEM-EDX analysis in the present study demonstrated clear differences between SG and DSG in surface morphology, including particle size and shape, as well as in elemental composition, particularly sulfur content. Sulfate quantification and FTIR spectroscopy further confirmed the presence of sulfur in both SG and DSG, verifying their sulfated nature. Notably, degradation to a lower molecular weight was associated

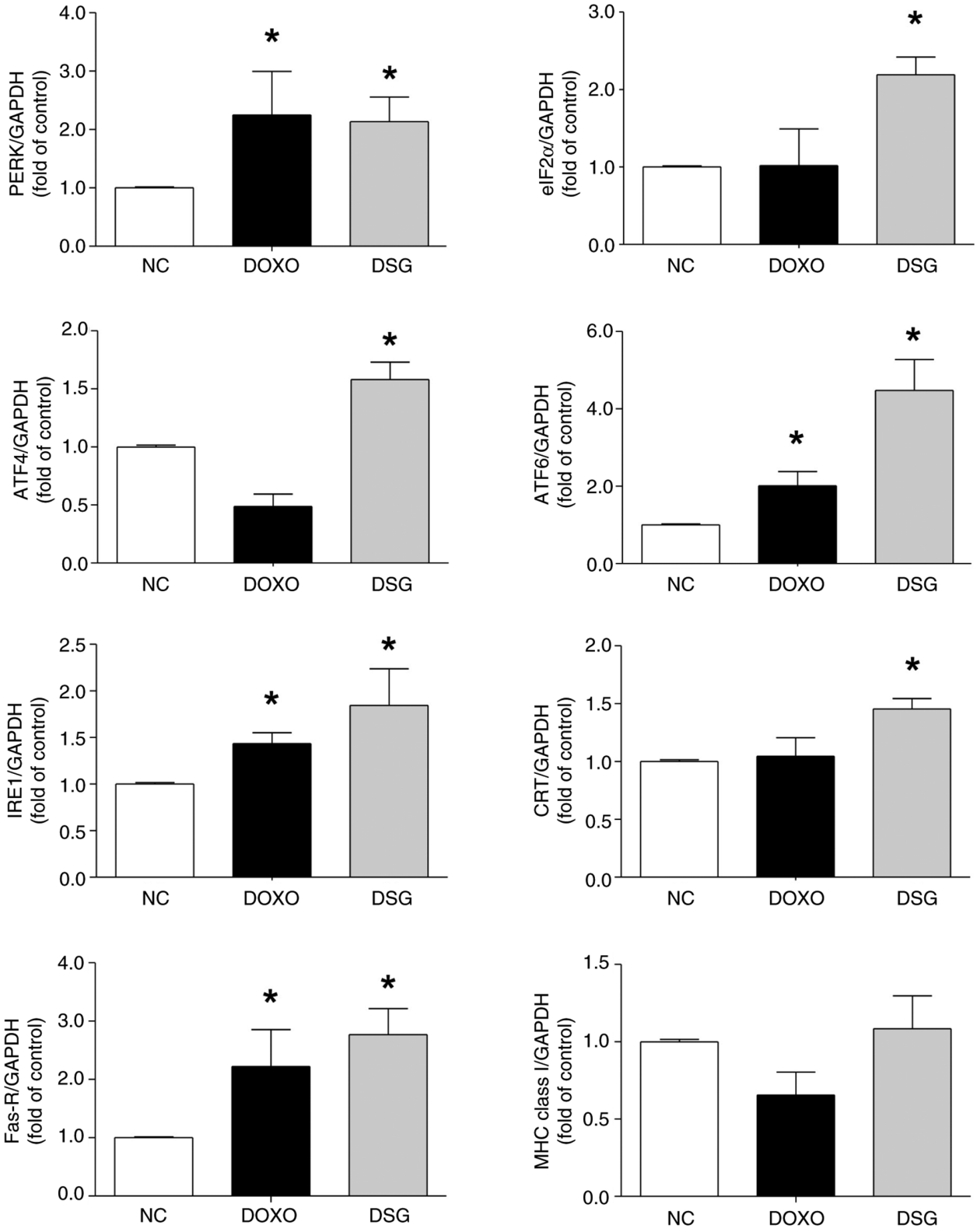

Figure 7. mRNA expression levels of PERK, eIF2α, ATF4, ATF6, IRE1, CRT, Fas-R and MHC class I in MDA-MB-231 cells treated with DOXO and DSG, as assessed by reverse transcription quantitative PCR and normalized to GAPDH. Results are presented as the mean±standard error of the mean (n=3) from three independent experiments. *P<0.05 indicates a statistically significant difference compared with the NC group. PERK, protein kinase RNA-like endoplasmic reticulum kinase; ATF, activating transcription factor; IRE1, inositol-requiring enzyme 1; eIF2α, eukaryotic initiation factor 2 α subunit; DSG, degraded sulfated galactan; NC, normal control; DOXO, doxorubicin; CRT, calreticulin; Fas-R, Fas receptor; MHC, major histocompatibility complex.

with increased sulfate content within the polysaccharide structure (33). These findings were consistent with previous studies on seaweed-derived sulfated polysaccharides, which reported that molecular weight and chemical composition strongly influence surface morphology and physicochemical properties (34,35).

The cytotoxic effects of SG and DSG on normal breast epithelial MCF-10A cells and triple-negative breast cancer MDA-MB-231 cells were evaluated and compared with those of DOXO, an extensively used anticancer drug and a well-established inducer of ICD (36,37). SG and DSG significantly reduced the viability of MDA-MB-231 cells while having no detectable effect on MCF-10A cell viability, whereas DOXO reduced viability in both cell lines. These findings were consistent with the notable morphological changes and increased membrane permeability observed in MDA-MB-231 cells after treatment. Together, these results indicated that SG and DSG exert selective cytotoxicity toward cancer cells while sparing normal cells (38). This pattern aligns with previous studies that demonstrated sulfated polysaccharides from *Padina tetrastromatica* exhibit no cytotoxic effects on normal cells at concentrations up to 2,000 μg/ml (39). Similarly, SG derivatives at concentrations of 500 and 1,000 μg/ml were cytotoxic to MCF-7 breast cancer cells but not to L929 normal fibroblasts (9). The selective anticancer activity of SG and DSG may reflect differences in cellular metabolism, surface receptor expression and intracellular signaling pathways between normal and cancer cells (40).

Cell morphological alterations and increased membrane permeability are often associated with elevated ROS generation induced by natural products used in cancer therapy (41). For example, *Artemisia monosperma* extracts exert cytotoxic effects on human colorectal carcinoma HCT-116 cells by inducing ROS overproduction, leading to notable morphological changes and membrane blebbing (42). Similarly, sulfated polysaccharides derived from *Padina tetrastromatica* induce morphological alterations in HeLa cells through ROS-mediated mitochondrial membrane depolarization and dysfunction (43), consistent with the present study observation that DSG increased ROS generation in MDA-MB-231 cells. By contrast, SG did not elevate ROS levels in MDA-MB-231 cells, suggesting that the observed membrane damage was not primarily ROS-mediated. This effect may instead be associated with increased membrane permeability resulting, at least in part, from disruption of cytoskeletal proteins such as actin. Proteolytic degradation of cytoskeletal components can compromise plasma membrane integrity and lead to alterations in cell morphology (44). Furthermore, treatment with DSG, characterized by lower-molecular weight and higher sulfate content, exhibits enhanced biological activity compared with SG, indicating a positive association between its structural features and bioactivity (45). Molecular weight and sulfate content are key determinants of the biological activity of sulfated polysaccharides (29). Low-molecular weight sulfated polysaccharides generally exhibit improved anticancer effects due to enhanced solubility, tissue penetration and cellular uptake, leading to greater inhibition of cancer cell proliferation, induction of apoptosis and suppression of tumor progression compared with the native form of sulfated polysaccharides (46). Additionally, higher sulfate content has been associated with increased bioactivity, as evidenced by greater inhibition of colony formation in moderately sulfated fucoidans compared with low-sulfated forms (47). Consistent with these findings, DSG likely exerts stronger anticancer activity by more effectively interacting with cell surface molecules and/or enhancing its penetration and uptake in MDA-MB-231 cells.

The impact of DSG treatment on the ultrastructure of MDA-MB-231 cells was further examined using TEM analysis. DSG-treated cells exhibited notable cytoplasmic alterations, including prominent vacuolization, electron-dense inclusions and marked organelle disorganization, closely resembling the ultrastructural features observed in DOXO-treated cells. These changes are indicative of cellular stress and cytotoxicity (48). The present study findings were consistent with previous studies that demonstrated ultrastructural analysis of MDA-MB-231 cells exposed to nanoencapsulated tarin revealed accumulation of autophagosomes and damaged organelles (49). Similarly, DOXO-treated human breast adenocarcinoma cells have been reported to contain abundant abnormal vacuoles containing fibrous, heterogeneous and flocculent material (50).

Notably, the presence of prominent cytoplasmic vacuoles and electron-dense structures suggests autophagosome formation and lysosomal involvement, features commonly associated with ER stress-mediated ICD (15). ER stress can trigger autophagic flux while promoting the exposure and release of DAMPs, thereby enhancing tumor immunogenicity (14,15). In the present study, DSG upregulated CRT and Fas-R expression but did not alter MHC class I levels compared with control cells. CRT exposure is a canonical hallmark of ICD that facilitates phagocytic uptake of dying tumor cells (14), whereas increased Fas-R expression enhances tumor cell susceptibility to immune-mediated apoptosis (16,51). By contrast, MHC class I primarily governs antigen presentation to $CD8^+$ T cells and reflects adaptive immune recognition rather than serving as a direct marker of ICD (17). The absence of changes in MHC class I expression suggested that DSG preferentially activates ICD-related danger signaling and immune susceptibility pathways without extensively enhancing antigen presentation machinery.

Furthermore, low-molecular weight sulfated polysaccharides exhibit improved cellular accessibility and bioavailability, which facilitates robust activation of ICD-associated ER stress signaling pathways, including PERK-eIF2α-ATF4, IRE1 and ATF6 (15). Consistent with this mechanism, DSG significantly upregulated the transcription of ER stress- and ICD-related genes, including PERK, eIF2α, ATF4, ATF6, IRE1, CRT and Fas-R, supporting its role as an ICD inducer. In line with these findings, lentinan derived from shiitake mushrooms suppresses tumor growth by inducing autophagy and apoptosis in HT-29 tumor models, accompanied by marked ER stress activation (52). Sustained ER stress can ultimately drive cell death through cytotoxic autophagy and disruption of Ca^{2+} homeostasis via pathways such as PERK/ATF4/CHOP and IRE1α (53). Beyond polysaccharides, the flavonol glycoside afzelin induces ICD in lung cancer cells by activating ER stress and increasing ATP, high mobility group box 1 and CRT release (54). Similarly, extracts of *Marsdenia tenacissima* inhibit non-small cell lung cancer cell viability by concurrently activating ER stress (ATF6, glucose-regulated protein 78 kDa, ATF4, X-box binding protein 1s and CHOP) and ICD pathways (55). *Trametes robiniophila* Murr. (Huaier) has also been reported to promote ICD in triple-negative breast cancer cells

by enhancing CRT exposure, potentially through the circular RNA cytoplasmic linker associated protein 1/double-stranded RNA-dependent protein kinase/eIF2α signaling axis (56).

The present study demonstrated that DSG derived from *Gracilaria fisheri* selectively exerts mild cytotoxic effects on triple-negative breast cancer MDA-MB-231 cells while sparing normal MCF-10A cells. Of note, DSG effectively triggers ICD, likely through activation of ER stress-mediated pathways, highlighting a mechanistic association between its structural features and immunomodulatory antitumor activity. Mild to moderate cytotoxicity induced by DSG may still serve a key role in promoting ICD-associated signaling and immunomodulatory activity, rather than diminishing its therapeutic relevance. ICD is not solely dependent on extensive tumor cell killing but is primarily driven by the induction of cellular stress responses that lead to the emission of DAMPs (14,15). In this context, mild cytotoxic stress caused by DSG may be sufficient to activate ER stress pathways, particularly the PERK-eIF2α axis, which is closely associated with CRT exposure on the cell surface, a key hallmark of ICD (15). These signals collectively enhance dendritic cell recruitment, antigen uptake and subsequent T-cell-mediated antitumor immunity. Notably, sulfated polysaccharides have also been reported to directly modulate immune cell functions, including macrophage activation and cytokine production, suggesting that their antitumor effects may arise from a combined action of tumor cell stress induction and immune system stimulation (57,58). Therefore, even in the presence of only mild cytotoxicity, DSG may still effectively contribute to anticancer immunity by functioning as an ICD-inducing immunomodulatory agent that amplifies both tumor-derived danger signals and host immune responses.

However, several limitations in the present study should be noted. Definitive confirmation of DSG-induced ICD will require additional functional assays, including co-culture of DSG-treated cancer cells with immune cells, phagocytosis assays and immune cell-mediated cytotoxicity assays. Furthermore, confirmatory experiments, such as the use of ROS scavengers (for example, N-acetylcysteine), PERK inhibition or gene knockdown, are warranted to verify that DSG triggers ICD through activation of ER stress-mediated pathways. Further studies are also warranted to determine whether DSG induces ICD in other breast cancer subtypes or additional cancer types and whether these effects can be reproduced *in vivo*. Addressing these points will be key to advancing DSG toward translational and clinical application in the future.

Acknowledgements

We would like to thank Dr Dylan Southard, International Affairs, Khon Kaen University International College, Thailand for language editing of the manuscript.

Funding

The present study received grants from the Khon Kaen University Faculty of Medicine, Thailand (grant no. IN69033) and Mahasarakham University Faculty of Medicine, Thailand (grant no. Med.Msu 01/09/2566).

Availability of data and materials

The data generated in the present study may be requested from the corresponding author.

Authors' contributions

TR, YP, KW and CP conceived and designed the present study. TR, YP, WS, JP and CP conducted the experiments. TR, WS, SS, JEA and CP performed the data analysis. TR, WS, SS and CP drafted the manuscript. TR, KW and CP revised and finalized the manuscript. TR and CP obtained funding, managed the project and confirm the authenticity of all the raw data. All authors read and approved the final manuscript.

Ethics approval and consent to participate

Not applicable.

Patient consent for publication

Not applicable.

Competing interests

The authors declare that they have no competing interests.

References

1. Sung H, Ferlay J, Siegel RL, Laversanne M, Soerjomataram I, Jemal A and Bray F: Global cancer statistics 2020: GLOBOCAN estimates of incidence and mortality worldwide for 36 cancers in 185 countries. CA Cancer J Clin 71: 209-249, 2021.
2. Łukasiewicz S, Czeczelewski M, Forma A, Baj J, Sitarz R and Stanisławek A: Breast cancer-epidemiology, risk factors, classification, prognostic markers, and current treatment strategies-an updated review. Cancers (Basel) 13: 4287, 2021.
3. Mun EJ, Babiker HM, Weinberg U, Kirson ED and Von Hoff DD: Tumor treating fields: A fourth modality in cancer treatment. Clin Cancer Res 24: 266-275, 2018.
4. Vijayalakshmi M, Meganathan S, Surendhar SK, Umamaheswari A and Prabu SL: Exploring the systematic anticancer mechanism in selected medicinal plants: A review. Oncol Adv 2: 141-147, 2024.
5. Armonavičius D, Maruška A, Jakštys B, Stankevičius M, Drevinskas T, Bimbiraitė-Survilienė K, Čaplikaitė M, Ihara H, Takafuji M, Skrzydlewska E, *et al*: Evaluation of the anticancer activity of medicinal plants predominantly accumulating ellagic acid compounds. Antioxidants (Basel) 14: 1339, 2025.
6. Guo R, Chen M, Ding Y, Yang P, Wang M, Zhang H, He Y and Ma H: Polysaccharides as potential anti-tumor biomacromolecules-A review. Front Nutr 9: 838179, 2022.
7. Habtemariam S: *Trametes versicolor* (Synn. *Coriolus versicolor*) polysaccharides in cancer therapy: Targets and efficacy. Biomedicines 8: 135, 2020.
8. Sae-Lao T, Tohtong R, Bates DO and Wongprasert K: Sulfated galactans from red seaweed *gracilaria fisheri* target EGFR and inhibit cholangiocarcinoma cell proliferation. Am J Chin Med 45: 615-633, 2017.
9. Phanphak J, Somintara S, Sakaew W, Senarai T, Kovensky J, Wongprasert K and Rudtanatip T: Sulfated galactan derivatives from *Gracilaria fisheri* suppress the proliferation of MCF7 breast cancer cells by inducing cell cycle arrest. World Acad Sci J 7: 77, 2025.
10. Van Allen EM, Miao D, Schilling B, Shukla SA, Blank C, Zimmer L, Sucker A, Hillen U, Foppen MHG, Goldinger SM, *et al*: Genomic correlates of response to CTLA-4 blockade in metastatic melanoma. Science 350: 207-211, 2015.

11. Schmid P, Cortes J, Pusztai L, McArthur H, Kümmel S, Bergh J, Denkert C, Park YH, Hui R, Harbeck N, *et al*: Pembrolizumab for early triple-negative breast Cancer. N Engl J Med 382: 810-821, 2020.
12. Peng K, Zhao X, Fu YX and Liang Y: Eliciting antitumor immunity via therapeutic cancer vaccines. Cell Mol Immunol 22: 840-868, 2025.
13. Fabian KP, Kowalczyk JT, Reynolds ST and Hodge JW: Dying of stress: Chemotherapy, radiotherapy, and small-molecule inhibitors in immunogenic cell death and immunogenic modulation. Cells 11: 3826, 2022.
14. Arimoto KI, Miyauchi S, Liu M and Zhang DE: Emerging role of immunogenic cell death in cancer immunotherapy. Front Immunol 15: 1390263, 2024.
15. Han Y, Tian X, Zhai J and Zhang Z: Clinical application of immunogenic cell death inducers in cancer immunotherapy: Turning cold tumors hot. Front Cell Dev Biol 12: 1363121, 2024.
16. Szarynska M, Olejniczak A, Wierzbicki P, Kobiela J, Laski D, Sledzinski Z, Adrych K, Guzek M and Kmiec Z: FasR and FasL in colorectal cancer. Int J Oncol 51: 975-986, 2017.
17. Wu K and Fong L: CD4+ T cells help myeloid-mediated killing of immune-evasive tumors. Trends Cancer 9: 777-779, 2023.
18. Pradhan B, Rout L and Ki JS: Immunomodulatory and anti-inflammatory and anticancer activities of porphyran, a sulfated galactan. Carbohydr Polym 301: 120326, 2023.
19. Liu W, Shen M, Li J and Xie J: Structure-activity relationships of sulfated polysaccharides in inflammatory bowel disease: Sources, mechanisms, and therapeutic potential. Carbohydr Polym 372: 124574, 2026.
20. Khongthong S, Theapparat Y, Roekngam N, Tantisuwanno C, Otto M and Piewngam P: Characterization and immunomodulatory activity of sulfated galactan from the red seaweed *gracilaria fisheri*. Int J Biol Macromol 189: 705-714, 2021.
21. Rudtanatip T, Somintara S, Sakaew W, ElAbid J, Cano ME, Jongsomchai K, Wongprasert K and Kovensky J: Sulfated galactans from *gracilaria fisheri* with supplementation of octanoyl promote wound healing activity in vitro and in vivo. Macromol Biosci 22: e2200172, 2022.
22. Wongprasert K, Rudtanatip T and Praiboon J: Immunostimulatory activity of sulfated galactans isolated from the red seaweed gracilaria fisheri and development of resistance against white spot syndrome virus (WSSV) in shrimp. Fish Shellfish Immunol 36: 52-60, 2014.
23. Livak KJ and Schmittgen TD: Analysis of relative gene expression data using real-time quantitative PCR and the 2(-delta delta C(T)) method. Methods 25: 402-408, 2001.
24. Patel MA, Manna S, Vo A, Xu X, Conti DS, Choi S, Kozak D and Zheng J: Scanning electron microscope (SEM) coupled with energy dispersive X-ray spectroscopy (EDS)-a potential analytical tool for physicochemical characterization of API in complex drug formulations. Microsc Microanal 26: 2254-2255, 2020.
25. Wang J, Sun D, Huang L, Wang S and Jin Y: Targeting reactive oxygen species capacity of tumor cells with repurposed drug as an anticancer therapy. Oxid Med Cell Longev 2021: 8532940, 2021.
26. Zhao H, Zhao Y, Zhang S, Wang Z, Yu W, Dong N, Yang X, Zhang X, Sun Q, Hao X and Ren X: Effects of immunogenic cell death-inducing chemotherapeutics on the immune cell activation and tertiary lymphoid structure formation in melanoma. Front Immunol 15: 1302751, 2024.
27. B J and R R: A critical review on pharmacological properties of sulfated polysaccharides from marine macroalgae. Carbohydr Polym 344: 122488, 2024.
28. Nagahawatta DP, Liyanage NM, Jayawardena TU, Yang F, Jayawardena HHACK, Kurera MJMS, Wang F, Fu X and Jeon YJ: Functions and values of sulfated polysaccharides from seaweed. Algae 38: 217-240, 2023.
29. Kang J, Jia X, Wang N, Xiao M, Song S, Wu S, Li Z, Wang S, Cui SW and Guo Q: Insights into the structure-bioactivity relationships of marine sulfated polysaccharides: A review. Food Hydrocoll 123: 107049, 2022.
30. Yue JR, Lu JM, Fan QF, Sun P, Li YJ, Zhou SL, Wang XY, Niu JM, Xu YK and Zhou J: Comparative study of the structural characteristics and bioactivity of polysaccharides extracted from *aspidopterys obcordate* hemsl. using different solvents. Molecules 28: 7977, 2023.
31. Zhang M, Zhao P, Ochir S, Bai W, Lu J, Dan M, Bo S and Chen C: Sulfated modification, characterizations, anti-oxidant and immunostimulatory activities of a polysaccharide from arnebia euchroma (royle) johnst. Roots. Results Chem 17: 102624, 2025.
32. Olasehinde TA, Mabinya LV, Olaniran AO and Okoh AI: Chemical characterization of sulfated polysaccharides from gracilaria gracilis and ulva lactuca and their radical scavenging, metal chelating, and cholinesterase inhibitory activities. Int J Food Prop 22: 100-110, 2019.
33. Gong P, Wang M, Guo Y, Long H, Wang Z, Cui D, Yao W, Yang W, Chen F and Xie J: Structure characterization, in vitro antioxidant and anti-tumor activity of sulfated polysaccharide from *siraitia grosvenorii*. Foods 12: 2133, 2023.
34. Tang L, Chen Y, Jiang Z, Zhong S, Chen W, Zheng F and Shi G: Purification, partial characterization and bioactivity of sulfated polysaccharides from grateloupia lívida. Int J Biol Macromol 94: 642-652, 2017.
35. Netanel Liberman G, Ochbaum G, Mejubovsky-Mikhelis M, Bitton R and Malis Arad S: Physicochemical characteristics of the sulfated polysaccharides of the red microalgae dixoniella grisea and porphyridium aerugineum. Int J Biol Macromol 145: 1171-1179, 2020.
36. Kciuk M, Gielecińska A, Mujwar S, Kołat D, Kałuzińska-Kołat **Ż**, Celik I and Kontek R: Doxorubicin-An agent with multiple mechanisms of anticancer activity. Cells 12: 659, 2023.
37. Cardador CM, de Castro TB, de Castro RJA, Bocca AL, Camargo LC, Pacheco TA, Muehlmann LA and Longo JPF: Doxorubicin-induced immunogenic cell death impairs tumor progression and distant metastasis in a 4T1 breast cancer tumor model. Curr Pharm Des 30: 2493-2504, 2024.
38. Blagosklonny MV: Selective protection of normal cells from chemotherapy, while killing drug-resistant cancer cells. Oncotarget 14: 193-206, 2023.
39. Jose GM, Raghavankutty M and Kurup GM: Attenuation of hydrogenperoxide-induced oxidative damages in L929 fibroblast cells by sulfated polysaccharides isolated from the edible marine algae *padina tetrastromatica*. J Bioact Compat Polym 34: 150-162, 2019.
40. Akhtar MJ, Ahamed M, Alhadlaq HA, Alrokayan SA and Kumar S: Targeted anticancer therapy: Overexpressed receptors and nanotechnology. Clin Chim Acta 436: 78-92, 2014.
41. Muchtaridi M, Az-Zahra F, Wongso H, Setyawati LU, Novitasari D and Ikram EHK: Molecular mechanism of natural food antioxidants to regulate ROS in treating cancer: A review. Antioxidants (Basel) 13: 207, 2024.
42. Farshori NN, Al-Sheddi ES, Al-Oqail MM, Al-Massarani SM, Al-Jassas EA, Ahmad J, Saquib Q, Wahab R, Al-Khedhairy AA and Siddiqui MA: *Artemisia monosperma* induces ROS-mediated cell death in human colorectal carcinoma cells via modulating apoptotic genes. J King Saud Univ Sci 35: 102763, 2023.
43. Jose GM, Raghavankutty M and Kurup GM: Sulfated polysaccharides from *Padina tetrastromatica* induce apoptosis in HeLa cells through ROS triggered mitochondrial pathway. Process Biochem 68: 197-204, 2018.
44. Nakajima K, Takakura H, Shimizu Y and Ogawa M: Changes in plasma membrane damage inducing cell death after treatment with near-infrared photoimmunotherapy. Cancer Sci 109: 2889-2896, 2018.
45. Wang Y, Xing M, Cao Q, Ji A, Liang H and Song S: Biological activities of fucoidan and the factors mediating its therapeutic effects: A review of recent studies. Mar Drugs 17: 183, 2019.
46. Liyanage NM, Dissanayake DS, Li Y, Ko KY, Nagahawatta DP and Jeon YJ: Sulfated polysaccharides in cancer therapy: A focus on algal-derived bioactive. Mar Drugs 24: 131, 2026.
47. Trung DT, Surits VV, Zueva AO, Cao HTT, Shevchenko NM, Ermakova SP and Thinh PD: Anticancer activity in vitro of sulfated polysaccharides from the brown alga *spatoglossum vietnamense*. Molecules 29: 4982, 2024.
48. Perrotta I: Live and let die: Analyzing ultrastructural features in cell death. Ultrastruct Pathol 49: 1-19, 2025.
49. Cardoso RV, Pereira PR, Freitas CS, Mattos ÉBA, Silva AVF, Midlej VDV, Vericimo MA, Conte-Júnior CA and Paschoalin VMF: Tarin-loaded nanoliposomes activate apoptosis and autophagy and inhibit the migration of human mammary adenocarcinoma cells. Int J Nanomed 18: 6393-6408, 2023.
50. Rembiałkowska N, Dubińska-Magiera M, Sikora A, Szlasa W, Szewczyk A, Czapor-Irzabek H, Daczewska M, Saczko J and Kulbacka J: Doxorubicin assisted by microsecond electroporation promotes irreparable morphological alternations in sensitive and resistant human breast adenocarcinoma cells. Appl Sci 10: 2765, 2020.
51. Sica M, Roussel M and Legembre P: CD95/Fas stoichiometry in future precision medicine. Cell Death Differ 32: 1570-1577, 2025.

52. Zhang Y, Liu Y, Zhou Y, Zheng Z, Tang W, Song M, Wang J and Wang K: Lentinan inhibited colon cancer growth by inducing endoplasmic reticulum stress-mediated autophagic cell death and apoptosis. Carbohydr Polym 267: 118154, 2021.
53. Fan J, Zhu J, Zhu H, Zhang Y and Xu H: Potential therapeutic target for polysaccharide inhibition of colon cancer progression. Front Med (Lausanne) 10: 1325491, 2024.
54. Xia L, Xu X, Li M, Zhang X and Cao F: Afzelin induces immunogenic cell death against lung cancer by targeting NQO2. BMC Complement Med Ther 23: 381, 2023.
55. Yuan Y, Guo Y, Guo ZW, Hao HF, Jiao YN, Deng XX and Han SY: Marsdenia tenacissima extract induces endoplasmic reticulum stress-associated immunogenic cell death in non-small cell lung cancer cells through targeting AXL. J Ethnopharmacol 314: 116620, 2023.
56. Li C, Wang X, Chen T, Li W, Zhou X, Wang L and Yang Q: Huaier induces immunogenic cell death *via* circCLASP1/PKR/eIF2α signaling pathway in triple negative breast cancer. Front Cell Dev Biol 10: 913824, 2022.
57. Bhuyan PP, Nayak R, Patra S, Abdulabbas HS, Jena M and Pradhan B: Seaweed-derived sulfated polysaccharides; The new age chemopreventives: A comprehensive review. Cancers (Basel) 15: 715, 2023.
58. Wang Y, Luo J, Xu C, Hu D, Li Y, Ye Y, Yang J, Chen X, Li C and Zhu K: Recent advance in marine polysaccharides: Structure, anti-inflammatory mechanisms, and functional applications. Mar Drugs 24: 129, 2026.